Multi-Tracer Guided PET Image Reconstruction

Sam Ellis, Andrew Mallia, Colm J. McGinnity, Gary J. R. Cook, and Andrew J. Reader

***Abstract*—Multi-tracer positron emission tomography (PET) has the potential to enhance PET imaging by providing complementary information from different physiological processes. However, one or more of the images may present high levels of noise. Guided image reconstruction methods transfer information from a guide image into the PET image reconstruction to encourage edge-preserving noise reduction. In this work we aim to reduce noise in poorer quality PET datasets via guidance from higher quality ones by using a weighted quadratic penalty approach. In particular, we applied this methodology to [^{18}F]fluorodeoxyglucose (FDG) and [^{11}C]methionine imaging of gliomas. 3D simulation studies showed that guiding the reconstruction of methionine datasets using pre-existing FDG images reduced reconstruction errors across the whole-brain (-8%) and within a tumour (-36%) compared to maximum likelihood expectation-maximisation (MLEM). Furthermore, guided reconstruction outperformed a comparable non-local means filter, indicating that regularising during reconstruction is preferable to post-reconstruction approaches. Hyperparameters selected from the 3D simulation study were applied to real data, where it was observed that the proposed FDG-guided methionine reconstruction allows for better edge preservation and noise reduction than standard MLEM. Overall, the results in this work demonstrate that transferring information between datasets in multi-tracer PET studies improves image quality and quantification performance.**

***Index Terms*—positron emission tomography, PET image reconstruction, guided reconstruction, regularisation, multi-tracer PET**

I. Introduction

POSITRON emission tomography (PET) allows the observation and quantification of various specific biological processes *in vivo* due to a) the high sensitivity of the imaging modality, and b) the wide range of available radio-labelled compounds (also known as radiotracers) that have been designed to target a wide range of functional and molecular processes.

There are a number of clinical and research situations where combining information from two or more radiotracers provides additional useful information. For example, in the imaging of brain tumours, the complementary information obtained from PET images using [^{18}F]fluoro-deoxyglucose (FDG) for glucose metabolism imaging and a protein synthesis and/or protein transport radiotracer such as [^{11}C]methionine (methionine) can improve the detection of malignant gliomas [1], [2]. Another example is the potential use of both FDG and [^{11}C]raclopride in the differential diagnosis of Parkinson's disease, progressive supranuclear palsy, and multiple system atrophy [3]. One final example is in the imaging of complementary neurotransmitter systems in the brain using different radiotracers, a topic of interest, for instance, in the exploration of the interaction between the glutamate and dopamine receptors in various neurological conditions [4], [5].

However, some of the radiotracers used in these contexts produce highly noisy images due to a range of factors including low injected dose or low specific uptake. In particular, the short half life of ^{11}C means that relatively short delays in scanning can considerably increase image noise levels for many specialised radiotracers.

Achieving noise reduction is one of the recurring themes of the PET image reconstruction field. When using relatively simple methods that seek images to only explain the measured data, such as the well-known maximum likelihood expectation-maximisation (MLEM) algorithm [6], PET image reconstruction often converges to noisy estimates. Therefore, regularisation methods to mitigate this effect have been studied intensively for many years [7]–[11].

In particular, guided image reconstruction methods use an external source of information to regularise the reconstruction of PET images. For example, using the images from another imaging modality, such as co-registered magnetic resonance (MR) images, allows PET images to be smoothed within regions that are expected to be uniform based on the prior images. A wide range of MR-guided PET image reconstruction techniques have been proposed [12]–[22], generally with the aim of reducing PET image noise and improving PET image resolution by preserving edges. MR-guidance has received a lot of attention due to the wide applicability and ubiquity of MR imaging and the recent development of simultaneous PET-MR scanners. Furthermore, the broad variety of MR acquisition sequences allows for many MR image contrasts that can be used for the guidance of PET image reconstructions [21].

However, MR-guidance of PET image reconstruction is not always appropriate or possible, particularly when imaging protocols do not include an MR scan. In these cases, it would be beneficial if other, higher quality, PET images could take the place of MR images and provide guidance for the reconstruction of noisy PET datasets. The application of guided reconstruction methodologies to the context of multi-tracer PET protocols in this way has not, to the best of

Submitted to IEEE Transactions on Radiation and Plasma Medical Sciences. This work was funded by the King's College London & Imperial College London EPSRC Centre for Doctoral Training in Medical Imaging [EP/L015226/1] and supported by both the EPSRC [EP/M020142/1] and the Wellcome EPSRC Centre for Medical Engineering at King's College London [WT 203148/Z/16/Z]. C. J. McGinnity is supported by the MRC grant [MR/N013042/1]. Patient data was acquired at the King's College London and Guy's and St Thomas' PET Centre through the Transforming Outcomes and Health Economics Through Imaging (TOHETI) programme. In accordance with the EPSRC's policy framework on research data, figures and data supporting this study are openly available at https://doi.org/10.5281/zenodo.1308883.

S. Ellis and A. J. Reader are with the School of Biomedical Engineering and Imaging Sciences, King's College London. A. Mallia, C. J. McGinnity, and G. J. R. Cook are with the School of Biomedical Engineering and Imaging Sciences, King's College London, and the King's College London and Guy's and St Thomas' PET Centre.

the authors' knowledge, been proposed before, although we have previously proposed the use of guided reconstruction in longitudinal contexts where the patient is scanned more than once with the same radiotracer [23]. This work demonstrates the principle of guided reconstruction in the multi-tracer PET case, investigating the specific case of FDG/methionine imaging of brain tumours. Often the reconstructed methionine images are very noisy and require large amounts of post-reconstruction smoothing to obtain clinically useful images. On the other hand, the FDG images generally exhibit high contrast and low noise. This work investigates the use of the higher quality FDG images to guide the reconstruction of the lower quality methionine data. To achieve this guidance, a weighted quadratic maximum *a posteriori* (MAP) objective function was used, where the weights are derived from a pre-existing FDG image, under the assumption that FDG and methionine distributions are structurally similar (i.e. that edges in FDG images correspond reasonably well to those in methionine images). A 3D simulation study was performed to explore the effects of the various parameters of the proposed reconstruction method, showing reduced reconstruction error and superior tumour quantification compared to standard MLEM reconstructions. Furthermore, preliminary tests to validate the simulation results on real patient data were seen to reinforce the noise reduction and edge-preservation benefits of the proposed reconstruction approach.

II. Theory

Regularised PET image reconstruction methods typically utilise a maximum *a posteriori* approach, where the objective function to be maximised is given by:

$$\Phi(\boldsymbol{\theta}) = L(\boldsymbol{\theta};\boldsymbol{m}) - \beta U(\boldsymbol{\theta}), \tag{1}$$

where $L(\boldsymbol{\theta};\boldsymbol{m})$ is the Poisson log-likelihood of an image vector, $\boldsymbol{\theta}$, giving rise to the measured data vector, $\boldsymbol{m}$. To perform a guided image reconstruction, the guidance information can be encoded in the penalty term $U(\boldsymbol{\theta})$ and the relative importance of this guidance compared to the data consistency (log-likelihood) term is defined by the value of the parameter β, also known as the penalty strength. Note that with $\beta = 0$, the reconstruction problem simplifies to maximum likelihood estimation, as solved by the MLEM algorithm.

One method of including this guidance information from other medical images into the reconstruction of a PET dataset is to use the weighted quadratic penalty [24], given by:

$$U(\boldsymbol{\theta}) = \frac{1}{4}\sum_{j=1}^{J}\sum_{k\in\mathcal{N}_j} w_{jk}\left(\theta_j - \theta_k\right)^2. \tag{2}$$

This penalty considers the pair-wise intensity differences between each voxel j and each of its neighbours, k, and performs a weighted sum of the square of each of these differences. In effect, the weights w_{jk} encode which voxels will be forced to have small intensity differences (high w_{jk}), and which ones are allowed to be more different (low w_{jk}). By calculating w_{jk} from a prior image, information from that image about which voxels are visually similar can be built into PET image reconstruction, allowing noise reduction and edge-preservation compared to standard PET image reconstruction methods.

In this work, we calculate these prior weights using Gaussian kernel functions, similar to those used by [18], [23], [25] and [22]:

$$w_{jk} = \exp\left(\frac{-\left\|\boldsymbol{f}_j - \boldsymbol{f}_k\right\|^2}{2\sigma_f^2}\right)\exp\left(\frac{-\left\|\boldsymbol{r}_j - \boldsymbol{r}_k\right\|^2}{2\sigma_s^2}\right), \tag{3}$$

where $\boldsymbol{f}_j$ is the feature vector for voxel j, $\boldsymbol{r}_j$ is the spatial location of voxel j, and σ_f and σ_s are parameters which control the widths of the two kernels. The first kernel is based on feature vectors, which in this work are $p\times p\times p$ patches from the prior image arranged as $p^3\times 1$ column vectors. Note that in this work the feature vectors are normalised by the standard deviation of each element across the image, according to [25], so that:

$$f_{j,m} = \frac{\hat{f}_{j,m}}{\mathrm{SD}_m\left(\{\boldsymbol{f}_j\}_{j=1}^{J}\right)}, \tag{4}$$

where $\hat{\boldsymbol{f}}_j$ are the unnormalised feature vectors, and $\mathrm{SD}_m\left(\{\boldsymbol{f}_j\}_{j=1}^{J}\right)$ is the standard deviation of the mth element of the feature vectors over all voxels. This normalisation allows σ_f to be a unitless quantity, while σ_s is expressed in the same units as the spatial distance between $\boldsymbol{r}_j$ and $\boldsymbol{r}_k$. By measuring the Euclidean distance between patch-based features in this way, it is possible to quantify the *a priori* similarity between the corresponding voxels.

Sparsification of guidance weights in PET image reconstruction is performed in order to reduce computational costs and to reduce the effect of spurious similarities. In the Bowsher prior [12], sparsification is achieved by keeping only the B most similar voxels for each voxel and setting these similarities to 1, while all other weights are set to 0 [12]. In the kernel method approach proposed by Wang and Qi [25], sparsification was proposed via the use of k-nearest neighbours or the threshold-based ε-ball method. In this work, we opt for a maximum-value sparsification method, where after calculation of all w_{jk}, only the n_{Max} maximum values are kept for each voxel j, and all others are set to be zero.

To maximise the objective function in equation 1 we utilise the modified expectation maximisation approach of De Pierro [26]. The use of a surrogate for the penalty in the maximisation step allows for a separable iterative update formula in terms of each voxel separately. Explicitly, the update formula is given by:

$$\theta_j^{(n+1)} = \frac{-A_j^{(n)} + \sqrt{\left(A_j^{(n)}\right)^2 + 4C_jB_j^{(n)}}}{2C_j}, \tag{5}$$

where

$$A_j^{(n)} = \sum_{i=1}^{I} p_{ij} - \beta\sum_{k\in\mathcal{N}_j} w_{jk}\left(\theta_j^{(n)} + \theta_k^{(n)}\right), \tag{6}$$

$$B_j^{(n)} = \theta_{j,\mathrm{EM}}^{(n+1)}\sum_{i=1}^{I} p_{ij}, \tag{7}$$

and

$$C_j = 2\beta\sum_{k\in\mathcal{N}_j} w_{jk}. \tag{8}$$

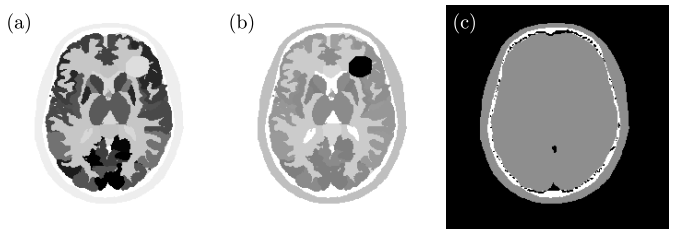

Fig. 1. High resolution (a) FDG and (b) methionine ground truth images for the 3D simulation study to characterise the effects of each hyperparameter listed in Table I. Note the tumour in the inferior aspect of the right frontal lobe (images shown in neurological orientation). (c) the attenuation map used for all simulations, showing three voxel classes: air, water and bone.

Note that p_{ij} are the elements of the system matrix, incorporating the effects of the geometric projection, attenuation and normalisation, and $\theta_{j,\text{EM}}^{(n+1)}$ is the expectation maximisation update used in standard MLEM, given by:

$$\theta_{j,\text{EM}}^{(n+1)} = \frac{\theta_j^{(n)}}{\sum_{i=1}^{I} p_{ij}} \sum_{i=1}^{I} p_{ij} \frac{m_i}{q_i\left(\boldsymbol{\theta}^{(n)}\right)}, \tag{9}$$

where $\boldsymbol{q}\left(\boldsymbol{\theta}^{(n)}\right)$ is the expected mean of the data using the current image estimate $\boldsymbol{\theta}^{(n)}$.

III. Experimental Methods

To evaluate the effect of guiding methionine PET image reconstructions with FDG images we performed a 3D simulation study. Guided reconstruction performance was measured as a function of the reconstruction hyperparameters and compared to standard MLEM reconstructions followed by both Gaussian and FDG-derived non-local-means filters. Following this simulation study, the proposed method was applied to real FDG/methionine data acquired on a Siemens Biograph mMR PET-MR scanner (Siemens Healthcare, Erlangen, Germany).

Data simulation and image reconstruction were implemented in MATLAB (MathWorks, MA, USA), using in-house Siddon-based mMR projectors [27]. Vendor-provided software was used to obtain normalisation factors and scatter and randoms estimates for the real data reconstructions. Attenuation factors for the real data were calculated using the vendor-provided ultra-short echo time MR-based attenuation maps and the same in-house geometric projectors used for reconstruction.

A. 3D Simulation Study

Two ground truth 3D brain images were generated from a freely available software phantom [28], with the contrasts adjusted to emulate FDG and methionine scans. The matrix size for the ground truth images was $688 \times 688 \times 254$, with a voxel size of $1.04313 \times 1.04313 \times 1.015625\,\text{mm}^3$. A tumour was introduced into the ground truth images, extending across the border between white and grey matter in the inferior aspect of the right frontal lobe (figure 1). In the FDG image, the tumour was hypo-intense with an intensity of 60% that of adjacent white matter, and in the methionine image the tumour was hyper-intense with a tumour to grey matter ratio of 2:1.

Using these two ground truth images, Siemens Biograph mMR data was simulated for each, using the same data generation pipeline. First, each ground truth image was blurred by a Gaussian filter of full-width-at-half-maximum (FWHM) of 4.3 mm [29] before projecting them into mMR standard sinogram space. Attenuation sinograms were produced using the segmented attenuation map (figure 1(c)), using the following tissue/value pairs for the linear attenuation coefficient: air, $0\,\text{cm}^{-1}$; water, $0.096\,\text{cm}^{-1}$; and bone, $0.172\,\text{cm}^{-1}$ [30]. Normalisation factors from a real mMR scan were then applied. Scattered events were modelled as a smoothed copy of the noise-free forward projection of the blurred images, and randoms were modelled as uniform sinograms. The noise levels and scatter and randoms fractions were adjusted so that the final FDG dataset contained 300 M counts, with 20% scatter and 30% randoms, and the final methionine dataset contained 70 M counts, with 20% scatter and 25% randoms.

To produce the prior image to be used to guide the reconstruction of the methionine dataset, the FDG dataset was reconstructed into the standard mMR $344 \times 344 \times 127$ image grid with a voxel size of $2.08626 \times 2.08626 \times 2.03125\,\text{mm}^3$, using 100 iterations of MLEM, and then smoothed by a 4 mm FWHM Gaussian kernel. This FDG prior image was used to calculate the weights in equation 2 in order to guide the reconstruction of the methionine images into the same image grid. For the simulation study, to reduce the large parameter space of the reconstructions, all feature vectors were $3 \times 3 \times 3$ cubic patches arranged as 27×1 vectors, and all neighbourhoods, $\mathcal{N}_j$, were $5 \times 5 \times 5$. Therefore the guided methionine reconstructions were a function of β, n_{Max}, σ_f, and σ_s. To explore the parameter space, a baseline value for each of these variables was defined (see table I), and each one was then varied between a minimum and maximum value in turn (column 3 of table I). These FDG-guided MAPEM reconstructions were run to 200 iterations of equation 5, initialised with one iteration of standard MLEM to avoid convergence artefacts at the axial edges of the field-of-view.

Reconstruction error was quantified by using the regional mean absolute error (MAE) metric:

$$\text{MAE}_\Omega = \frac{100\%}{N_\Omega} \sum_{j \in \Omega} \frac{\left|\theta_j - \theta_j^{\text{Ref}}\right|}{\theta_j^{\text{Ref}}}, \tag{10}$$

where Ω is the region in which error is to be measured, N_Ω is the number of voxels in that region, and $\boldsymbol{\theta}^{\text{Ref}}$ is the reference image against which error is being calculated. For the 3D simulation study, MAE was calculated in methionine images

TABLE I
Parameters used for the reconstruction of methionine datasets in the 3D hyperparameter characterisation simulation study. Each parameter had a baseline value which was held constant while each of the other parameters were varied in turn with the range shown in the final column.

Parameter	Baseline value	Range (min–max)
β	15000	5000–25000
n_{Max}	15	5–125
σ_f	4	0–8
σ_s	4 mm	0–8 mm

in the whole-brain region and in the tumour alone, in both cases using a linearly interpolated downsampled version of the ground truth image as $\boldsymbol{\theta}^{\text{Ref}}$. Additionally, the contrast recovery coefficient (CRC) of the tumour was measured as:

$$\text{CRC} = \frac{\bar{T} - \bar{B}}{\bar{B}}, \tag{11}$$

where $\bar{T}$ is the mean voxel intensity within the tumour, and $\bar{B}$ is the mean voxel intensity in a white matter background region. The standard deviation (SD) of the voxel intensities within the tumour and the white matter background region were also measured.

For comparison to the FDG-guided MAPEM methionine reconstructions, the same datasets were also reconstructed with 200 iterations of MLEM and filtered post-reconstruction with Gaussian filters of varying FWHM. In addition, the MLEM images were filtered with non-local-means (NLM) filters corresponding to the same FDG-derived weights used in the MAPEM approach (denoted hereafter as FDG-NLM). In practice, this involved the multiplication of the MLEM reconstruction image vector with the weights w_{jk} inserted into a sparse $J \times J$ matrix and appropriately normalised.

In order to evaluate the effect of the convergence of the guidance FDG image on the quality of the reconstructed methionine images, guidance weights were calculated from 4 mm smoothed FDG reconstructions using 50, 100 and 200 iterations of MLEM. These weights were calculated using the baseline hyperparameter values listed in Table I. The methionine dataset was then reconstructed with each of these three sets of weights in turn, and the resultant images compared.

Finally, to assess the performance of the proposed reconstruction method in cases of strong disagreement between the guiding FDG PET image and the methionine image, a mismatch test was carried out using a second pair of phantoms in which there was a smaller, methionine-unique tumour embedded within the grey matter. The corresponding region in the FDG image was uniform in intensity. The methionine data were reconstructed with both MLEM with a 5 mm Gaussian smooth and FDG-guided methionine with parameters based on the hyperparameter characterisation experiments detailed above.

B. Real Data Preliminary Study

Following the simulation study, the proposed methodology was applied to a real FDG/methionine scan pair from a single suspected glioma patient who was scanned in a Siemens Biograph mMR PET-MR scanner (Siemens Healthcare, Erlangen, Germany) with both radiotracers in the same day. The methionine scan was performed first, with an injected activity of 337 MBq and a scan duration of 11.4 min, beginning at 40 min post-injection. Fifty-six min after the methionine injection, 233 MBq of FDG was injected into the patient, who was then scanned for 11.7 min at 54 min post-injection. The final FDG dataset contained 381 M counts, and the methionine dataset contained 73.7 M.

The FDG-guided methionine image reconstruction pipeline for the real data is shown in figure 2. The FDG dataset was first reconstructed into the standard $344 \times 344 \times 127$ image grid

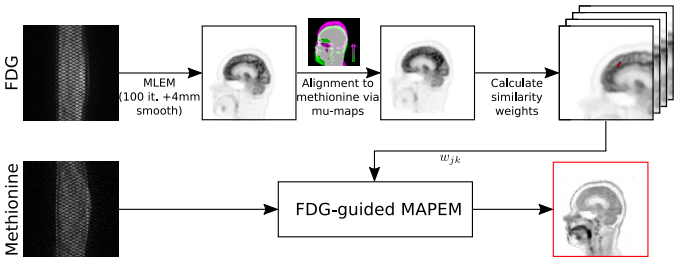

Fig. 2. Data processing pipeline used for the FDG-guided image reconstruction of the real methionine dataset. First, the FDG image was reconstructed with 100 iterations of MLEM and then smoothed with a Gaussian kernel of FWHM 4 mm. This reconstructed image was then transformed to the methionine image space using rigid-body transformations estimated from the attenuation maps, before the similarity weights w_{jk} were calculated. The final step involved inputting these weights into the MAPEM reconstruction algorithm alongside the measured methionine data to produce FDG-guided MAPEM reconstructions.

with 100 iterations of MLEM followed by a 4 mm Gaussian smooth. Following this, the FDG image was transformed to the methionine image space via a rigid-body transformation estimated using the MATLAB Image Processing Toolbox from the simultaneously acquired MR-based attenuation maps. The transformed FDG image was then used to calculate the set of weights w_{jk} as described above, using parameter values selected based on the 3D simulation study results. These weights were then input into the reconstruction of the methionine dataset (i.e. 200 iterations of equation 5) to produce the output FDG-guided methionine images. For comparison purposes, two additional sets of guidance weights were calculated from the co-acquired T1-weighted MR image and a previously acquired aligned computed tomography (CT) image using the same hyperparameter values, and the methionine dataset reconstructed using these weights.

Finally, a validation experiment was carried out on the real data in order to investigate the extent to which guiding a methionine image reconstruction with an FDG image affects the structure of the output methionine image. Ideally this would be achieved by using a high-counts methionine dataset to produce a reference image against which lower counts reconstructions using FDG-guided MAPEM or MLEM could be compared. However, due to the counts-limited nature of the available methionine dataset, this experimental approach was not possible. Instead, a similar methodology was employed whereby a low-noise methionine image was produced by reconstructing the data with 200 iterations of MLEM into a coarse image grid ($115 \times 115 \times 42$) at three times the standard mMR voxel size listed above. Counts-reduced methionine datasets were then generated by randomly removing counts from the original methionine sinogram according to a Bernoulli process, with the probability of removal equal to the expected proportion of counts remaining. In this way, methionine datasets with 10% and 20% the original data were generated. The original FDG dataset was reconstructed into the same coarse image grid to calculate the weights for FDG-guided MAPEM. The counts-reduced methionine datasets were then reconstructed with 200 iterations of FDG-guided MAPEM and Gaussian filtered MLEM. Reconstruction error was quantified by measuring the

MAE between reconstructed counts-reduced images and the original 100% MLEM reconstruction in brain voxels within a single slice.

IV. Results

A. 3D Simulation Study

In order to compare the methods at their best possible performance in terms of whole-brain MAE, a preliminary test was performed to ascertain the optimum FWHM for the Gaussian filtered MLEM methionine reconstruction. This value was found to be 5 mm, which produced a whole-brain MAE of 19.3%. Figure 3 shows the image metrics as a function of penalty strength, β, for the FDG-guided MAPEM. As β increases, the whole-brain MAE in the FDG-guided MAPEM reconstructions reduces (figure 3(a)), with $\beta = 10000$ providing the same whole-brain MAE as MLEM with a 5 mm Gaussian smooth. In this case, using the FDG-NLM filter on the MLEM reconstruction produced higher whole-brain MAE than a Gaussian filter. When considering the trade-off between tumour SD and tumour mean (figure 3(b)), it is apparent that using FDG-guided MAPEM allows greater reduction in the tumour noise while maintaining the quantification of the tumour mean compared to both the FDG-NLM and Gaussian filtered MLEM reconstructions. The FDG-guided MAPEM method also outperforms MLEM with either a Gaussian or FDG-NLM filter in terms of reconstruction error in both the tumour only and the rest of the brain (3(c)). Specifically, comparing FDG-guided MAPEM with the baseline parameter values (i.e. $\beta = 15000$ in figure 3) to the 5 mm Gaussian filtered MLEM, the MAE is reduced by 8% across the whole-brain, and 36% in the tumour. Finally, FDG-guided MAPEM produces higher tumour CRC at a given noise level when compared to the post-reconstruction filtered MLEM reconstructions (figure 3(d)).

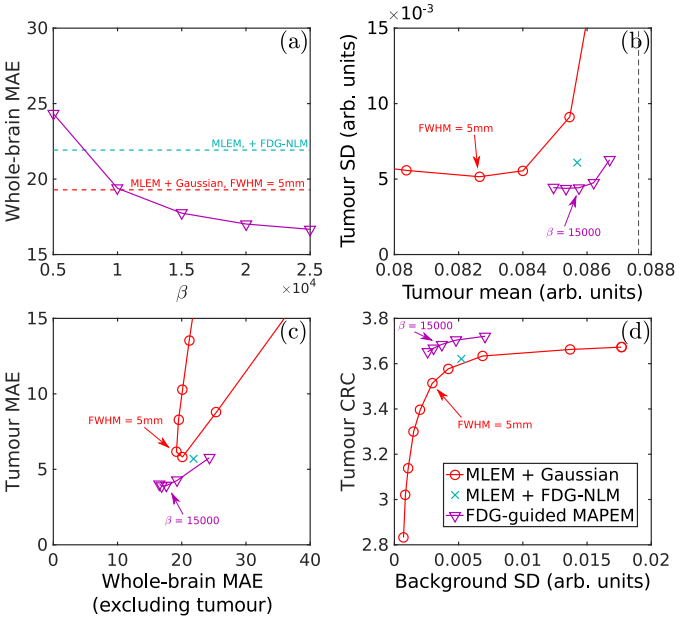

Fig. 3. Effect of the penalty strength β on (a) the whole-brain MAE, (b) tumour standard deviation vs tumour mean, (c) whole-brain MAE excluding tumour vs tumour MAE, and (d) tumour contrast recovery coefficient vs background standard deviation for FDG-guided MAPEM. Also shown are results obtained from using MLEM followed by Gaussian smooths and MLEM followed by the FDG-NLM filter. Note that all parameters (other than β) were set to the baseline values given in table I for both FDG-guided MAPEM and the FDG-NLM filter. Dashed grey line in (b) shows the tumour mean in the ground truth image.

These results are reflected in the reconstructed images (figure 4). The 5 mm Gaussian filtered MLEM image achieves good levels of noise reduction, but at the cost of blurred edges, including around the border of the tumour. The FDG-NLM filtered MLEM image suffers less from edge degradation, but contains an artefact-like noise pattern which makes the image less visually appealing than the Gaussian filtered MLEM. Compared to both of these images, the FDG-guided MAPEM image exhibits low noise across the image while also maintaining the appearance of edges.

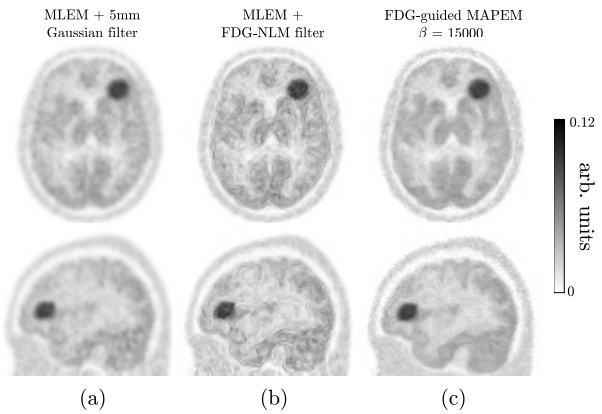

Fig. 4. Example reconstructed images for (a-b) MLEM followed by (a) a 5 mm Gaussian filter, (b) an FDG-NLM filter, and (c) FDG-guided MAPEM with $\beta = 15000$. All undisplayed hyperparameters for the latter two methods took baseline values from table I. The FDG-guided MAPEM simultaneously outperforms the Gaussian filtered MLEM in terms of noise reduction and edge-preservation while avoiding the artefacts observed in the FDG-NLM filtered MLEM image.

When the number of maximum values retained in the weights matrix per voxel (n_{Max}) was varied, the FDG-NLM filtered MLEM results greatly improve (figure 5). At higher values of n_{Max} (> 40), using the FDG-NLM filter outperformed the FDG-guided MAPEM in terms of whole-brain MAE (figure 5(a)), with both methods providing lower MAE than the 5 mm Gaussian filtered MLEM image. When the tumour SD/mean tradeoff is considered though, it is apparent that the FDG-guided MAPEM performs better than the FDG-NLM filtered MLEM method by providing a higher tumour mean for fixed standard deviation for $n_{\text{Max}} < 20$ (figure 5(b)). This is reflected in a superior tradeoff between tumour CRC and background noise (figure 5(d)). In terms of total tumour

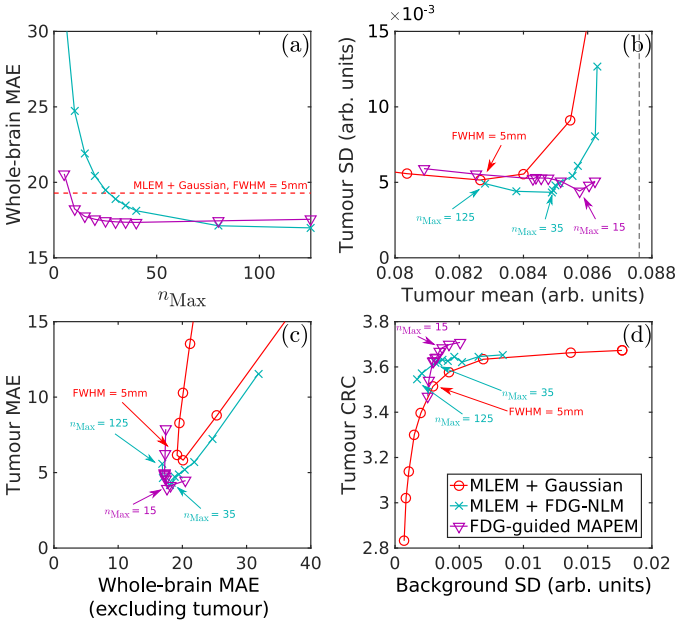

Fig. 5. Image metrics as a function of n_{Max} for FDG-NLM filtered MLEM images and FDG-guided MAPEM. Also shown are results from Gaussian filtered MLEM. (a) Whole-brain MAE as a function of n_{Max} for FDG-NLM and FDG-guided MAPEM, with 5 mm Gaussian filtered MLEM shown as a reference. (b) Tradeoff between tumour SD and tumour mean as a function of n_{Max} for FDG-NLM filtered MLEM and FDG-guided MAPEM, and as a function of FWHM for Gaussian smoothed MLEM. (c) Tradeoff between tumour MAE and the MAE in the rest of the brain as a function of n_{Max} and FWHM for the competing methods. (d) Tradeoff between tumour CRC and background noise.

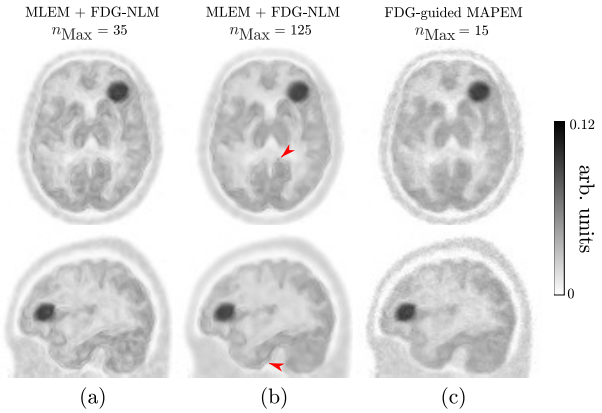

Fig. 6. Example reconstructed images from the investigation into the effect of the parameter n_{Max} on image quality for FDG-NLM filtered MLEM and FDG-guided MAPEM. (a) FDG-NLM filtered MLEM with $n_{\text{Max}} = 35$, (b) FDG-NLM filtered MLEM with $n_{\text{Max}} = 125$, and (c) FDG-guided MAPEM with $n_{\text{Max}} = 15$. Note that with a lower value of n_{Max} (i.e. less computational burden), the FDG-guided MAPEM produces images of equal or superior quality compared to the FDG-NLM filtered MLEM images. Arrows indicate examples of the FDG-NLM artefacts which remain even with $n_{\text{Max}} = 125$.

MAE against the MAE in the rest of the brain (figure 5(c)), the FDG-NLM filtered MLEM and the FDG-guided MAPEM perform similarly, with slightly lower errors from FDG-guided MAPEM.

When considering the reconstructed images (figure 6), the FDG-guided MAPEM is superior to the noise-matched FDG-NLM filtered MLEM with $n_{\text{Max}} = 35$, which retains some artefacts similar to those seen in figure 4. The FDG-NLM filtered image with $n_{\text{Max}} = 125$ produces an image which is less noisy than the FDG-guided MAPEM image, but visually is less appealing due to oversmoothing and some remaining artefacts (indicated by arrows).

Figure 7 shows the results of varying σ_f and σ_s. Beyond $\sigma_f = 2$ and $\sigma_s = 2$ mm, the FDG-guided MAPEM results are stable, outperforming MLEM with a 5 mm Gaussian filter and a FDG-NLM filter with any value of either σ_f or σ_s. The performances of both FDG-NLM filtered MLEM and FDG-guided MAPEM at high σ_f and σ_s are similar to their performances as shown in figure 3.

When the FDG dataset was reconstructed with 50 or 200 iterations of MLEM, instead of the 100 used above, the resultant prior images were visually similar (figure 8). The 50-iteration FDG prior (FDG_{50}) displays lower levels of noise than the 100-iteration FDG prior (FDG_{100}) and some blurring from being under-converged, and the 200-iteration prior (FDG_{200}) exhibits more noise, although this is mitigated by the subsequent 4 mm Gaussian smooth. The resulting FDG-guided methionine reconstructions all appear visually similar, and

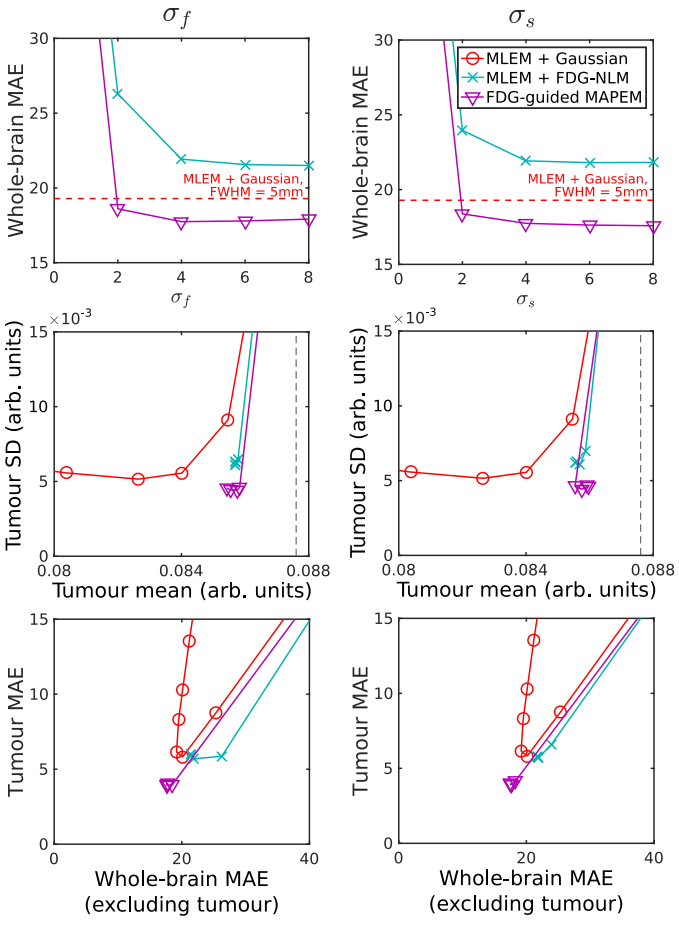

Fig. 7. Effect of the hyperparameters σ_f (left) and σ_s (right) on image metrics for FDG-guided MAPEM and FDG-NLM filtered MLEM, with all other parameters set to their baseline values as listed in table I. Also shown is Gaussian filtered MLEM. At σ_f and $\sigma_s \geq 4$, FDG-NLM filtered MLEM and FDG-guided MAPEM perform similarly to the results seen in figure 3.

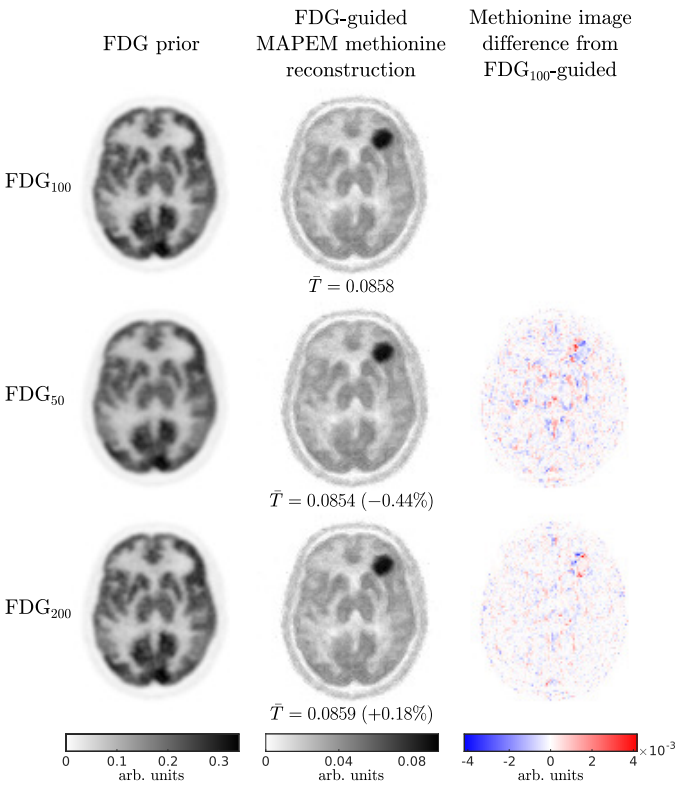

Fig. 8. The effect of changing the reconstruction of the FDG-prior on the FDG-guided MAPEM methionine reconstructions in simulated data. Left column: 4 mm smoothed FDG priors with 100, 50, and 200 iterations of MLEM (FDG_{100}, FDG_{50}, and FDG_{200} respectively); middle column: the corresponding FDG-guided methionine reconstructions; and right column: the difference between each methionine reconstruction and the FDG_{100}-guided methionine reconstruction. $\bar{T}$ denotes the measured tumour mean, and values in brackets denote the percentage difference from the FDG_{100}-guided tumour mean measurement.

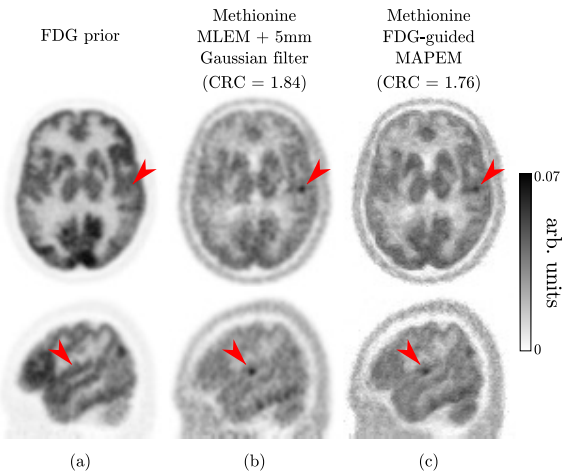

Fig. 9. Reconstructed images for the mismatch test. (a) the FDG prior, reconstructed with 100 iterations of MLEM followed by a 4 mm Gaussian smooth; (b) the methionine data reconstructed with 200 iterations of MLEM followed by a 5 mm Gaussian smooth; and (c) FDG-guided methionine reconstruction using the baseline hyperparameter values as listed in table I. Arrows indicate the location of the methionine-specific tumour, which was attenuated more by the FDG-guided reconstruction than the Gaussian smoothed MLEM reconstruction. This was reflected by a 4.3% reduction in tumour to white matter CRC.

the difference between them and the FDG_{100}-guided image is observed to be small, with a maximum difference in observed tumour mean of 0.44%. This difference was smaller for the FDG_{200}-guided methionine reconstruction, indicating that the difference in calculated weights is smaller when moving from 100 to 200 iterations for the prior compared to moving from 50 to 100 iterations.

On the other hand, when the tumour was changed for a methionine-specific tumour in the mismatch test, performing FDG-guided methionine image reconstruction was observed to attenuate the observed tumour intensity to a greater extent than that which was observed when using an MLEM reconstruction with a 5 mm Gaussian smooth (figure 9). This manifested as a 4.3% reduction in tumour to white matter CRC (from 1.84 using smoothed MLEM to 1.76 using FDG-guided MAPEM).

B. Real Data Preliminary Study

From the 3D simulation study, the baseline hyperparameter values were observed to produce good results overall, so that for the real FDG-guided MAPEM reconstructions these parameter values were used (as listed in table I). Figure 10 shows the reconstructed images for the real data case, including the aligned FDG prior image, the T1-weighted MR image acquired simultaneously with the methionine data, and the aligned CT image acquired prior to the PET-MR scan. Note that the MR and CT images have been resampled to the PET image grid, and that the CT has been contrast-enhanced using a 3D contrast limited adaptive histogram equalisation. It can be seen that the methionine image reconstructed using FDG-guided MAPEM is visually sharper than the 5 mm Gaussian filtered MLEM reconstruction, in agreement with the 3D simulation study results. Furthermore, the FDG-guided MAPEM reconstructions are sharper than both the CT- and MR-guided MAPEM reconstructions. This is particularly visible in the thalamus (figure 10(a)), where the FDG-guided MAPEM image exhibits a higher regional uptake than Gaussian filtered MLEM and both CT- and MR-guided reconstructions. The FDG-NLM filtered image exhibits strong artefacts similar to those seen in the 3D simulation study (figure 4). Importantly, when considering a region where there is a discrepancy between the FDG and the methionine images in the anterior temporal lobe (figure 10(b)), this is preserved in the FDG-guided MAPEM images.

When β is varied from 2000 to 18000 (figure 11), the effects of the penalty strength can be more clearly observed. There does not appear to be any change in the visual appearance of the radiotracer distribution as β increases, only an improvement in the noise characteristics of the images.

For the validation study using the coarse reconstructed image grid, the guidance hyperparameter values were set based on the baseline values used above. Since the voxel size increased by a factor of three, features were reduced from $3\times3\times3$ patches to single voxel values and the neighbourhoods were reduced from $5 \times 5 \times 5$ to $3 \times 3 \times 3$. σ_f was left equal to 4 since features are normalised, and σ_s was set to 8 mm to allow suitably large similarities between neighbouring voxels. n_{Max} was reduced from the previous baseline value of 15 to 3 in order to keep the same proportion of voxels in the weights

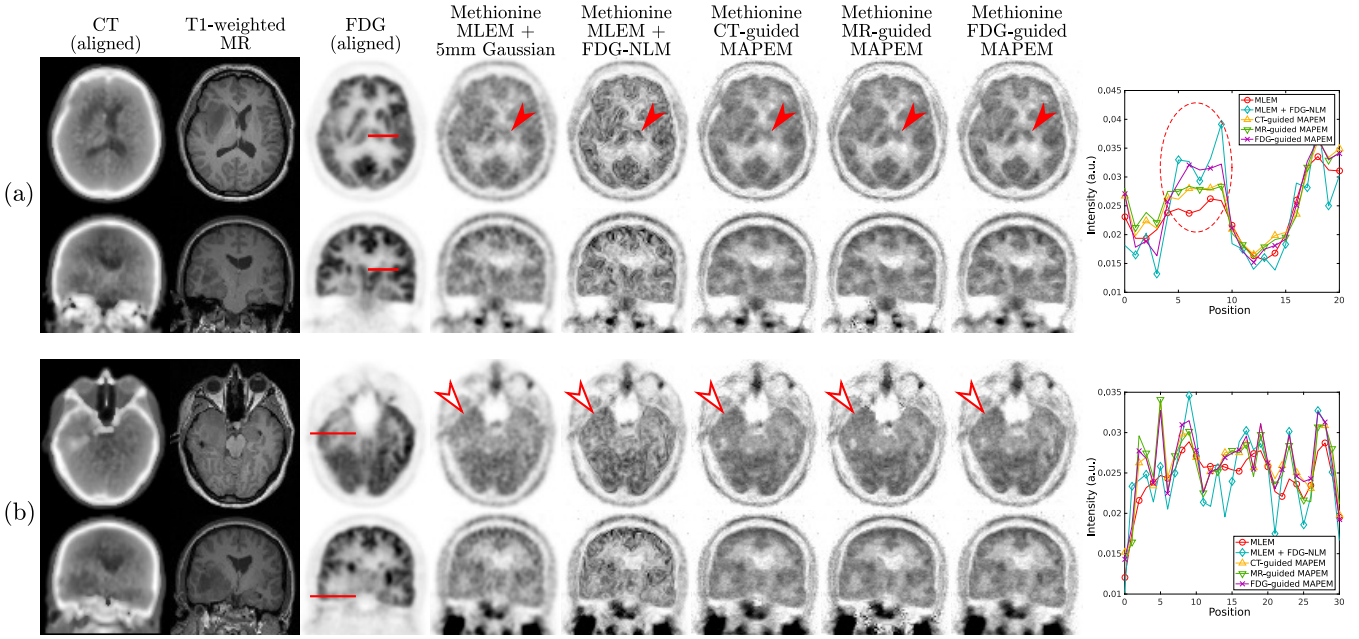

Fig. 10. Reconstructed images for the real data preliminary study. From left to right for both (a) and (b): previously acquired CT image, aligned and resampled to the methionine image grid and contrast-enhanced using a 3D contrast limited adaptive histogram equalisation; T1-weighted MR image acquired simultaneously with the methionine PET data, resampled to the methionine image grid; FDG data reconstructed with 100 iterations of MLEM, followed by a 4 mm Gaussian smooth and then aligned into the methionine image space; methionine data reconstructed with MLEM followed by a 5 mm Gaussian smooth; the same methionine data reconstructed with MLEM and then followed by FDG-NLM filtering; the methionine data reconstructed with CT-guided MAPEM; the methionine data reconstructed with MR-guided MAPEM; the methionine data reconstructed with FDG-guided MAPEM; and methionine image profiles as indicated by the lines superimposed on the FDG reconstructions. All methionine reconstructions were run to 200 iterations, and all guided reconstructions used the baseline hyperparameter values as given in Table I. (a) Increased uptake was observed in the thalamus when using the FDG-guided MAPEM compared to the Gaussian filtered MLEM and CT- and MR-guided reconstructions (filled arrows and circled in the profile). (b) A discrepancy between FDG and methionine uptakes is apparent (unfilled arrows), however the FDG-guided MAPEM allows good reconstruction of this region without any visible cross-talk.

$(15/125 \rightarrow 3/27)$, and β was varied between 250000 and 30000000 since redefining the voxel grid scales the value of the log-likelihood term.

Figure 12(a) shows the brain MAE in the analysed slice as a function of β, demonstrating that the optimum β value depends on the counts level of the dataset. Similarly, for Gaussian smoothed MLEM (figure 12(b)), the optimum smoothing level depends on the counts level. It can be seen that using FDG-guided MAPEM with 10% counts allows for MAE values similar to those obtained with MLEM using 20% counts. When considering the images at the best MAE values for each method/counts level combination, (figure 12(c)), FDG-guided MAPEM is observed to produce images that are visually less noisy than the counts-matched MLEM reconstruction. Furthermore, the structure in the FDG-guided MAPEM reconstruction is seen to agree with that present in the 100% counts image. Finally, the error maps obtained with the FDG-guided MAPEM (figure 12(d)) do not show any visible structure, supporting the observation that the use of the FDG-guidance did not introduce any visual artefacts into the reconstructed images.

V. Discussion

This work makes the novel proposal of using guidance information from one PET image in the reconstruction of another PET dataset produced using a different radiotracer. To evaluate the possible benefits of such a methodology, a 3D FDG/methionine brain tumour simulation study was performed to explore the parameter space of a weighted quadratically-penalised FDG-guided reconstructions and compare reconstructed images with MLEM with either a post-reconstruction Gaussian or FDG-derived NLM filter. Following this, a real FDG/methionine dataset pair were reconstructed with the proposed method and compared to post-reconstruction filtered MLEM and CT- and MR-guided MAPEM images.

In terms of the penalty strength β, it was observed that FDG-guided MAPEM outperformed post-reconstruction filtering methods in terms of reconstruction error in both the tumour and in the rest of the brain, indicating that FDG-guidance in a quadratic penalty achieves the noise reduction and edge-preservation that is desired. With increasing values of β, whole-brain error reduced (figure 3(a)), and was still reducing at the maximum β value tested (25000), implying that there is potentially a higher β value than provides a lower whole-brain MAE. Nevertheless, at $\beta = 25000$, the tumour mean value had already become considerably biased (figure 3(b)), indicating that a higher β value, while more optimal across the whole-brain, would be sub-optimal in the tumour compared to the other values tested in this work.

An unexpected observation from the results of varying β was that the FDG-NLM filtered MLEM reconstruction performed worse than applying a 5 mm Gaussian filter in terms of whole-brain error, despite the use of information from the FDG image in creating the NLM filter. The reason for this lies in the support of the filters; the FDG-derived NLM filter

had only $n_{\text{Max}} = 15$ non-zero elements, whereas the Gaussian filter had many more non-zero elements. Therefore, the noise reduction achieved by the Gaussian filters was superior to that obtained by using the FDG-NLM filter. This is supported by figure 5, where using the FDG-NLM filter with a higher value of n_{Max} allowed for reconstruction errors lower than those provided by the 5 mm Gaussian filter.

Conversely, since the FDG-guided MAPEM provides regularisation during the reconstruction process, smoothing is effectively applied at each iteration (according to equation 6) and so can propagate over the course of many iterations. This ensures that sufficient noise reduction can be achieved with a lower value of n_{Max}, without compromising edges or introducing the artefacts observed in the FDG-NLM reconstructions in figures 4 and 6. It is possible that alternative methods of using the same FDG guidance information, such as inter-iteration NLM filtering, or the use of FDG-derived spatial basis functions (c.f. [18], [19], [22]), could alleviate the problems we observed when using NLM filters, although such a comparison is beyond the scope of this work.

While β and n_{Max} were seen to have a strong impact on reconstructed image quality, the parameters σ_f and σ_s were observed to have a relatively small impact (figure 7). At sufficiently high values of each, the whole-brain MAE, tumour mean and SD, and tumour MAE were all stable, with results reflecting those seen in figure 3. This may be due to the baseline values chosen for the other parameters, particularly n_{Max}. Since the baseline value of n_{Max} was relatively low (15), the effect of the two kernel widths was limited; that is to say that once the maximum 15 values had been selected for each voxel, they were sufficiently similar to that voxel that widening the weights kernels would make no difference. Future work could account for this by repeating the analysis of the effects of σ_f and σ_s at various values of n_{Max}.

The reconstruction parameters of the FDG prior were also observed to have a relatively weak impact on the quality of the FDG-guided reconstructions (figure 8). The resultant methionine images appeared visually similar when using FDG priors reconstructed with 50, 100, or 200 iterations of MLEM followed by a 4 mm Gaussian smooth. This suggests that as long as the guiding image is of sufficient quality (i.e. has a sufficient number of measured counts), the calculated weights

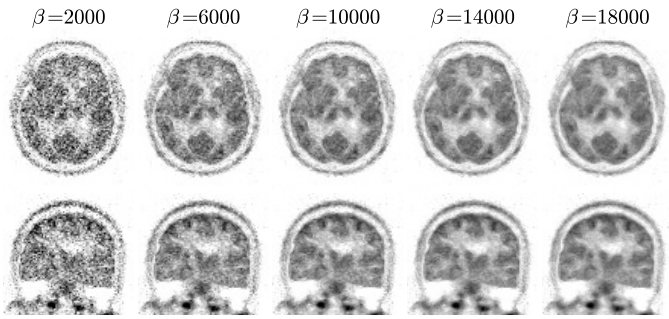

Fig. 11. Real data FDG-guided MAPEM reconstructions as a function of β, using the same weights parameters as were used in figure 10. Noise levels decrease as β increases, without visually affecting the pattern of distribution of the radiotracer.

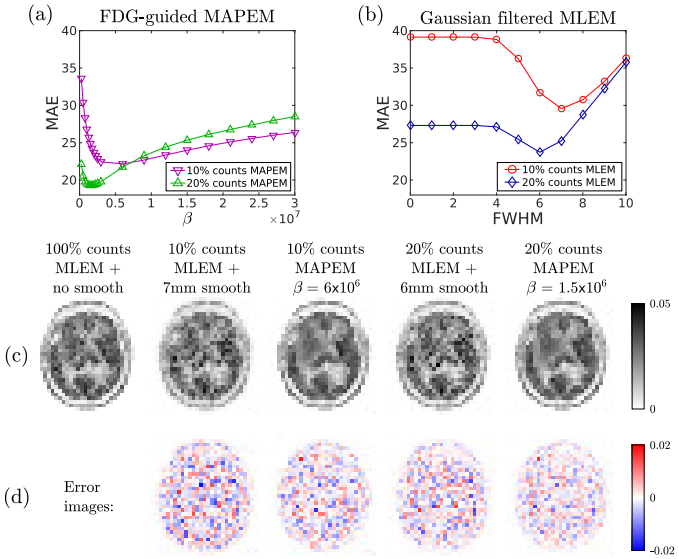

Fig. 12. Results of the validation experiment using real data reconstructed at a larger voxel size that was 3× the standard mMR voxel size. (a) Reconstruction MAE in the analysed slice relative to the 100% MLEM reference image as a function of β for FDG-guided MAPEM at both 10% and 20% counts levels, (b) the corresponding MAE values for MLEM with a varying Gaussian smooth, (c) reconstructed images at the best parameter value for FDG-guided MAPEM and MLEM for the two counts levels, with FDG-guided MAPEM exhibiting lower image noise than the corresponding MLEM reconstructions, and (d) the error maps for the the images in (c), showing that using FDG-guided MAPEM does not appear to introduce any structural artefacts into the error image.

will be similar, since the Gaussian smoothed MLEM image estimate will converge to a low-noise solution. Additional work could be carried out in the future to assess more fully this impact; in particular it would be important to know the minimum number of FDG counts that allow for reliable methionine image improvement in a given application before using the resulting FDG-guided methionine images in place of standard MLEM images.

Future work will also require parameter optimisation based on a larger number of patient datasets, evaluated in an application-specific manner with figures of merit and image quality metrics that relate more directly to the clinical need of the multi-tracer protocol in question. While MAE and other error-based metrics are useful for the preliminary evaluation of reconstruction methods in simulation studies, they can tend to prefer oversmoothed images (as seen in figures 5 and 6), and so can suggest a sub-optimal set of reconstruction parameters for a given clinical problem.

In general, when performing guided PET image reconstructions, care must be taken to avoid the so-called 'cross-talk' problem: where smoothing penalties are incorrectly translated from the guiding image into the image to be reconstructed, giving rise to the appearance of features that are not present in the true radiotracer distribution such as false edges. In the hyperparameter characterisation study performed in this work, the same anatomical boundary locations were used for both the FDG and methionine ground truth images (figure 1), potentially unfairly benefiting the FDG-guided MAPEM since there was a true close correspondence between the two images.

In fact, when a mismatch was introduced into the phantom by inserting a small methionine-specific tumour, this feature was blurred more in the FDG-guided image reconstruction than in the standard Gaussian smoothed MLEM reconstruction (figure 9). This result suggests that although the proposed method can perform well in some situations, it is inadvisable to use FDG-guidance when similar mismatches are possible. Therefore, before widespread use on clinical data, the application-specific hyperparameter characterisation mentioned above would be vital to ensure that the risk of attenuating methionine-specific features is limited. On the other hand, the fact that the images reconstructed from the real data display improvements with no visible cross-talk in regions where the radiotracer distributions differ (figure 10) indicates that FDG-guided MAPEM can be robust to the differing distributions of uptake for two radiotracers that correspond to distinct biological processes. This robustness was validated further by performing a counts reduction experiment whereby methionine reconstructions at 10% and 20% counts levels were compared to the MLEM reconstruction of the 100% counts dataset. However, due to the low counts levels in the original dataset, validation had to be performed at a larger voxel size to provide sufficient counts per voxel in the 100% counts reference image. Nevertheless, the results showed reduced reconstruction error relative to this reference image when using FDG-guided MAPEM compared to MLEM. The reconstructed images and the error maps did not show any visible structure that would be indicative of cross-talk between the datasets, reinforcing that the method is robust to cross-talk issues at least down to this voxel size. It would useful to repeat this experiment in future with a high-counts methionine dataset that allows for the same analysis to be repeated at the standard clinically used voxel size to verify that there are no smaller structures which are degraded by reconstructing methionine images with FDG-guidance.

Of course, the issue of validating guided reconstructions and avoiding cross-talk is not confined to the multi-tracer guided reconstruction case. MR-guided reconstruction, although being an established method for improving PET images, can also suffer, as observed in figure 10(a), where MR-guidance (as well as CT-guidance) blurred the thalamus relative to the FDG-guided reconstruction. This was due to the relatively weak MR contrast in this area, in comparison to the high-contrast FDG image. This suggests that although FDG images lack in resolution (particularly when smoothed post-reconstruction), their high contrast means that they are still useful in guiding the reconstruction of other PET datasets. While it is possible that additional pre-processing of MR images could improve the respective guided methionine reconstructions, this would be an area for future study, and one that has so far remained under-investigated in MR-guided PET image reconstruction. It should also be noted that by combining both FDG and MR (and even CT) information into a single, multi-modality prior, the methionine image could be improved even further; this would also need to be explored in future work.

In the previous discussion about the effects of cross-talk between the two datasets, it is assumed that the guidance image is perfectly aligned to the image to be reconstructed. In practice, artefacts could manifest as artificial edges if the prior image is systematically misaligned. In this work the registration problem was addressed by estimating rigid-body transformations from the pair of attenuation maps acquired with the PET datasets. This method worked well, with no artefacts present to suggest that a misalignment occurred. In brain scans such as those presented in this work, rigid-body alignment is an appropriate choice for modelling the deformation between two scans and the accuracy of the attenuation map based transformations is likely smaller than the PET resolution when all resolution degrading effects are considered. In order to apply the proposed methodology to other anatomical regions, more complex registrations may be required. These could be provided by estimating motion from co-acquired MR or CT images, or they could be estimated from the emission data in conjunction with other regularisation or prior information using joint emission and deformation estimation methods [31]–[33]. Alternatively, the proposed methodology could be applied to simultaneous dual-tracer PET protocols, where the dynamic nature of two radiotracers allows for the separation of their signals (e.g. [3]). In this case, the images from the two radiotracers should be automatically aligned, simplifying or even eliminating the alignment problem.

It is important to note that the weighted quadratic penalty is far from the only method for incorporating guidance information into a PET image reconstruction problem. Other notable alternatives include information theoretic anatomical priors [13], the parallel level sets prior [17], and basis function/reparameterisation approaches [18], [19], [22]. Previous work has attempted to compare the various guided reconstruction methods in the context of MR-guided PET image reconstruction [14], [17], [21], but it has proven difficult to fully characterise the wide range of available methods in terms of all relevant hyperparameters in an application-specific manner. Nonetheless, weighted quadratic penalties (particularly in the form of the Bowsher prior [12]) have been widely used due to their ease of implementation and relative robustness [14]. For this reason, in this work we have proposed multi-tracer guided PET image reconstruction using a weighted quadratic penalty only, although any of the aforementioned MR-guidance methods would be adaptable. A comparison of the performance of these alternative methods in the multi-tracer context remains for future work.

VI. Conclusion

Multi-tracer PET protocols utilise complementary information from different PET radiotracers to improve clinical and research studies. In these contexts, one or more radiotracer images may contain high levels of noise. This work proposes the use of higher quality PET images to guide the reconstruction of lower quality PET datasets. By using the high quality PET image to define which sets of voxels in the lower quality PET image are expected to have similar intensities, edge-preserving regularised image reconstruction can be performed in a manner similar to that used in MR-guided PET reconstruction. To evaluate the benefits of such a methodology, we focused on the specific case of glioma imaging, where using images from both FDG and methionine can be used to

improve diagnosis. High quality FDG images were used to derive inter-voxel similarity weights within neighbourhoods to guide a quadratically-penalised MAPEM reconstruction of the methionine datasets. 3D simulation studies showed lower errors in reconstructed methionine images when using FDG-guided MAPEM, and superior quantification in a tumour that was hypo-intense in terms of FDG uptake and hyper-intense in terms of methionine uptake. When applied to real patient data, similar improvements were seen across the image, and furthermore, the methionine-specific radiotracer distribution was maintained when using FDG guidance. Future work will involve further validation of the proposed methodology on greater numbers of real dataset pairs and extension of the methodology to other radiotracer pairings.

If the results of these future investigations replicate the improvements observed in this work, multi-tracer guided image reconstruction methods could have the potential to improve image quality via edge-preserving noise reduction across a wide range of clinical and research applications.

REFERENCES

[1] G. J. R. Cook *et al.*, "Normal variants, artefacts and interpretative pitfalls in PET imaging with 18-fluoro-2-deoxyglucose and carbon-11 methionine," *Eur. J. Nucl. Med.*, vol. 26, no. 10, pp. 1363–1378, 1999.

[2] J.-K. Chung *et al.*, "Usefulness of 11C-methionine PET in the evaluation of brain lesions that are hypo- or isometabolic on 18F-FDG PET," *Eur. J. Nucl. Med. Mol. Imaging*, vol. 29, no. 2, pp. 176–182, 2002.

[3] G. E. Fakhri *et al.*, "Dual-Tracer PET Using Generalized Factor Analysis of Dynamic Sequences," *Mol. Imaging Biol.*, vol. 15, no. 6, pp. 1536–1632, 2013.

[4] D. Pellegrino *et al.*, "Modulation of Dopaminergic and Glutamatergic Brain Function: PET Studies on Parkinsonian Rats," *J. Nucl. Med.*, vol. 48, no. 7, pp. 1147–1153, 2007.

[5] O. Howes *et al.*, "Glutamate and dopamine in schizophrenia: An update for the 21st century," *Journal of Psychopharmacology*, vol. 29, no. 2, pp. 97–115, 2015.

[6] L. A. Shepp and Y. Vardi, "Maximum Likelihood Reconstruction for Emission Tomography," *IEEE Trans. Med. Imaging*, vol. 1, no. 2, pp. 113–122, 1982.

[7] P. J. Green, "Bayesian Reconstructions from Emission Tomography Data Using a Modified EM Algorithm," *IEEE Trans. Med. Imaging*, vol. 9, no. 1, pp. 84–93, 1990.

[8] D. S. Lalush and B. M. W. Tsui, "Simulation Evaluation of Gibbs Prior Distributions for Use in Maximum *A Posteriori* SPECT Reconstructions," *IEEE Trans. Med. Imaging*, vol. 11, no. 2, pp. 267–275, 1992.

[9] V. Y. Panin *et al.*, "Total Variation Regulated EM Algorithm," *IEEE Trans. Nucl. Sci.*, vol. 46, no. 6, pp. 2202–2210, 1999.

[10] G. Wang and J. Qi, "Penalized Likelihood PET Image Reconstruction Using Patch-Based Edge-Preserving Regularization," *IEEE Trans. Med. Imaging*, vol. 31, no. 12, pp. 2194–2204, 2012.

[11] J. Jiao *et al.*, "Detail-Preserving PET Reconstruction with Sparse Image Representation and Anatomical Priors," in *Inf. Process. Med. Imaging 24th Int. Conf. IPMI 2015, Sabhal Mor Ostaig, Isle Skye, UK, June 28 - July 3, 2015, Proc.*, 2015, pp. 540–551.

[12] J. E. Bowsher *et al.*, "Utilizing MRI information to estimate F18-FDG distributions in rat flank tumors," in *IEEE Symposium Conference Record Nuclear Science 2004.*, vol. 4, 2004, pp. 2488–2492.

[13] S. Somayajula *et al.*, "PET Image Reconstruction Using Information Theoretic Anatomical Priors," *IEEE Trans. Med. Imaging*, vol. 30, no. 3, pp. 537–549, 2011.

[14] K. Vunckx *et al.*, "Evaluation of Three MRI-Based Anatomical Priors for Quantitative PET Brain Imaging," *IEEE Trans. Med. Imaging*, vol. 31, no. 3, pp. 599–612, 2012.

[15] B. Bai *et al.*, "MR-Guided PET Image Reconstruction," *Semin. Nucl. Med.*, vol. 43, no. 1, pp. 30–44, 2013.

[16] V. G. Nguyen and S. J. Lee, "Incorporating Anatomical Side Information Into PET Reconstruction Using Nonlocal Regularization," *IEEE Trans. Med. Imaging*, vol. 22, no. 10, pp. 3961–3973, 2013.

[17] M. J. Ehrhardt *et al.*, "PET Reconstruction With an Anatomical MRI Prior Using Parallel Level Sets," *IEEE Trans. Med. Imaging*, vol. 35, no. 9, pp. 2189–2199, 2016.

[18] W. Hutchcroft *et al.*, "Anatomically-aided PET reconstruction using the kernel method," *Phys. Med. Biol.*, vol. 61, no. 18, pp. 6668–6683, 2016.

[19] P. Novosad and A. J. Reader, "MR-guided dynamic PET reconstruction with the kernel method and spectral temporal basis functions," *Phys. Med. Biol.*, vol. 61, no. 12, pp. 4624–4645, 2016.

[20] M. S. Tahaei and A. J. Reader, "Patch-based image reconstruction for PET using prior-image derived dictionaries," *Phys. Med. Biol.*, vol. 61, no. 18, pp. 6833–6855, 2016.

[21] A. Mehranian *et al.*, "PET image reconstruction using multi-parametric anato-functional priors," *Phys. Med. Biol.*, vol. 62, no. 15, pp. 5975–6007, 2017.

[22] J. Bland *et al.*, "MR-Guided Kernel EM Reconstruction for Reduced Dose PET Imaging," *IEEE Trans. Rad. Plasma Med. Sci.*, vol. PP, no. 99, pp. 1–1, 2017.

[23] S. Ellis and A. J. Reader, "Kernelised EM Image Reconstruction for Dual-Dataset PET Studies," in *2016 IEEE Nuclear Science Symposium, Medical Imaging Conference and Room-Temperature Semiconductor Detector Workshop (NSS/MIC/RTSD)*, 2016, pp. 1–3.

[24] J. A. Fessler *et al.*, "Regularized Emission Image Reconstruction Using Imperfect Side Information," *IEEE Trans. Nucl. Sci.*, vol. 39, no. 5, pp. 1464–1471, 1992.

[25] G. Wang and J. Qi, "PET Image Reconstruction Using Kernel Method," *IEEE Trans. Med. Imaging*, vol. 34, no. 1, pp. 61–71, 2015.

[26] A. R. De Pierro, "A modified expectation maximization algorithm for penalized likelihood estimation in emission tomography," *IEEE Trans. Med. Imaging*, vol. 14, no. 1, pp. 132–137, 1995.

[27] M. A. Belzunce and A. J. Reader, "Assessment of the impact of modeling axial compression on PET image reconstruction," *Medical Physics*, vol. 44, no. 10, pp. 5172–5186, 2017.

[28] A. Rahmim *et al.*, "Accurate Event-Driven Motion Compensation in High-Resolution PET Incorporating Scattered and Random Events," *IEEE Trans. Med. Imaging*, vol. 27, no. 8, pp. 1018–1033, 2008.

[29] G. Delso *et al.*, "Performance Measurements of the Siemens mMR Integrated Whole-Body PET/MR Scanner," *J. Nucl. Med.*, vol. 52, no. 12, pp. 1914–1922, 2011.

[30] C. Burger *et al.*, "PET attenuation coefficients from CT images: experimental evaluation of the transformation of CT into PET 511-keV attenuation coefficients," *Eur. J. Nucl. Med. Mol. Imaging*, vol. 29, no. 7, pp. 922–927, 2002.

[31] M. W. Jacobson and J. A. Fessler, "Joint Estimation of Image and Deformation Parameters in Motion-Corrected PET," in *2003 IEEE Nuclear Science Symposium. Conference Record*, vol. 5, Oct 2003, pp. 3290–3294.

[32] M. Blume *et al.*, "Joint Reconstruction of Image and Motion in Gated Positron Emission Tomography," *IEEE Trans. Med. Imaging*, vol. 29, no. 11, pp. 1892–1906, 2010.

[33] F. Kalantari *et al.*, "Respiratory motion correction in 4D-PET by simultaneous motion estimation and image reconstruction (SMEIR)," *Phys. Med. Biol.*, vol. 61, no. 15, pp. 5639–5661, 2016.